HAL
open science

Lithological correction of chemical weathering proxies based on K, Rb, and Mg contents for isolation of orbital signals in clastic sedimentary archives

T. Matys Grygar, K. Mach, K. Hron, K. Fačevicová, Mathieu Martínez, C. Zeeden, P. Schnabl

To cite this version:

T. Matys Grygar, K. Mach, K. Hron, K. Fačevicová, Mathieu Martínez, et al.. Lithological correction of chemical weathering proxies based on K, Rb, and Mg contents for isolation of orbital signals in clastic sedimentary archives. Sedimentary Geology, 2020, 406, pp.105717. 10.1016/j.sedgeo.2020.105717 . insu-02885803

HAL Id: insu-02885803

https://insu.hal.science/insu-02885803v1

Submitted on 1 Jul 2020

HAL is a multi-disciplinary open access archive for the deposit and dissemination of scientific research documents, whether they are published or not. The documents may come from teaching and research institutions in France or abroad, or from public or private research centers.

L'archive ouverte pluridisciplinaire **HAL**, est destinée au dépôt et à la diffusion de documents scientifiques de niveau recherche, publiés ou non, émanant des établissements d'enseignement et de recherche français ou étrangers, des laboratoires publics ou privés.

Journal Pre-proof

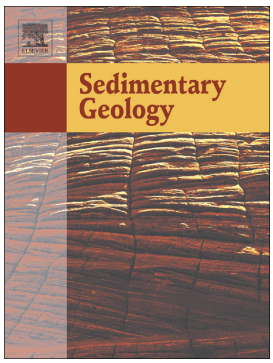

Lithological correction of chemical weathering proxies based on K, Rb, and Mg contents for isolation of orbital signals in clastic sedimentary archives

T. Matys Grygar, K. Mach, K. Hron, K. Fačevicová, M. Martinez, C. Zeeden, P. Schnabl

PII: S0037-0738(20)30132-9

DOI: https://doi.org/10.1016/j.sedgeo.2020.105717

Reference: SEDGEO 105717

To appear in: *Sedimentary Geology*

Received date: 22 April 2020

Revised date: 19 June 2020

Accepted date: 20 June 2020

Please cite this article as: T.M. Grygar, K. Mach, K. Hron, et al., Lithological correction of chemical weathering proxies based on K, Rb, and Mg contents for isolation of orbital signals in clastic sedimentary archives, *Sedimentary Geology* (2020), https://doi.org/10.1016/j.sedgeo.2020.105717

This is a PDF file of an article that has undergone enhancements after acceptance, such as the addition of a cover page and metadata, and formatting for readability, but it is not yet the definitive version of record. This version will undergo additional copyediting, typesetting and review before it is published in its final form, but we are providing this version to give early visibility of the article. Please note that, during the production process, errors may be discovered which could affect the content, and all legal disclaimers that apply to the journal pertain.

© 2020 Published by Elsevier.

Journal Pre-proof

Lithological correction of chemical weathering proxies based on K, Rb, and Mg contents for isolation of orbital signals in clastic sedimentary archives

T. Matys Grygar[a], K. Mach[b], K. Hron[c], K. Fačevicová[c], M. Martinez[d], C. Zeeden[e], P. Schnabl[f]

[a] Czech Academy of Sciences, Institute of Inorganic Chemistry, 250 68 Řež, Czech Republic

[b] North Bohemian Mines, j.s.c., 5. května 2013, 418 01 Bílina, Czech Republic

[c] Faculty of Science, Palacký University, 17. listopadu 12, 771 46 Olomouc, Czech Republic

[d] UMR 6118 Geosciences Rennes, Observatoire des Sciences de l'Univers Rennes, Université de Rennes 1, Campus de Beaulieu, 35042 Rennes Cedex, France

[e] LIAG, Leibniz Institute for Applied Geophysics, Stilleweg 2, Hannover, 30655, Germany

[f] Institute of Geology of the Czech Academy of Sciences, Rozvojová 269, 165 00 Prague, Czech Republic

Abstract

The extraction of palaeoenvironmental (palaeoclimatic) signals from the chemical composition of siliciclastic sediments is valuable for the reconstruction of past environments, particularly in continental basins. Here we test novel weathering proxies, which are less sensitive to lithological control than the previously used raw element ratios K/Al, K/Ti, and K/Rb: (1) local enrichment factors of K/Al, Mg/Al, and K/Rb, i.e., the element ratios corrected for grain size- and matrix composition using local background functions (Al/Si, Fe, and Ca as explanatory variables) and ordinary regression and (2) robust regression residuals of those element ratios based on isometric log-ratio coordinates of the most relevant "lithogenic" elements (Ca, Fe, Rb, Si, Zr) in the chemical composition. Chemical weathering proxies can be obtained from departures of chemical composition of sedimentary profiles from relationships with other chemical elements, in particular those with grain-size control. The resulting weathering proxies were examined for the Miocene deposits from the Most Basin, the

Czech Republic, which recorded one of the major warm episodes of the Cenozoic time – the Miocene Climatic Optimum. The performance of weathering proxies has been checked by (1) comparison of individual proposed proxies in one drill core HK930, (2) detailed analysis of orbital signals in the relevant compositional functions in HK930; and (3) lateral correlation of three cores HK930, DU7, and DO565 of the same basin. The novel proxies show lateral stability and orbital signatures of short eccentricity, obliquity, and precession, confirming their usefulness in palaeoenvironmental studies. Corrections for grain-size and carbonate contents should help to isolate climatic content from the weathering proxies, although in the studied sediments it weakened the precession component in the orbital signal, as grain-size proxies and other compositional data also carried orbital signals. We propose to consider these proxy ideas in palaeoclimatic reconstructions based on chemical weathering proxies.

Keywords: geochemistry; weathering proxies; robust statistics; log-ratio methodology; stratigraphy; cyclostratigraphy

Journal Pre-proof

1 Introduction

The chemical composition of sediments is among the most extensively used quantitative characteristic studied for palaeoenvironmental reconstructions. The sediment composition results from the interplay of geological provenance (parent rock composition – mineralogy, weathering resistance, and grain size of weathering products), weathering intensity in the source area, grain size control on particle transport, and geochemical and physical alterations of sediment particles before, during, and after deposition (Garzanti et al., 2011, 2013; Bloemsma et al., 2012; von Eynatten et al., 2016; Laceby et al., 2017; Deng et al., 2019). The isolation of individual driving factors from the overall chemical sediment composition is a persistent challenge for data pre-treatment, statistical processing, and interpretation. The interplay of named factors has long been discussed also for chemical weathering proxies (Garzanti et al., 2013; Hu et al., 2013; von Eynatten et al., 2016; Profe et al. 2016; Degeai et al. 2018). Isolation of the chemical weathering intensity is highly desirable in palaeoenvironmental studies based on sedimentary series. When provenance is constant, the major hindrance is the grain-size control of the weathering proxies (Guo et al., 2018; Sun et al., 2018b; Deng et al., 2019; Matys Grygar et al., 2019b; Bosq et al., 2020).

The grain size is a key to all aspects of the geochemical composition of sediments, as it is known from analysis of recent loose sediments (Bouchez et al., 2011; Lupker et al., 2011; von Eynatten et al., 2016; Laceby et al., 2017; Li et al., 2020). Even in such sediments, the grain-size control of chemical composition cannot be fully removed by sieving (Laceby et al., 2017), but it can be treated by geochemical normalisation, i.e., evaluation of chemical variations from element concentration ratios (Kersten and Smedes, 2002; Garzanti et al., 2013; Matys Grygar and Popelka, 2016; Matys Grygar et al., 2019b). Geochemical normalisation has been empirically verified in many case studies. It can be simplified for example by the quartz dilution effect, if the sediment was a mixture of fine particles of clay minerals and coarser quartz particles. In real sediments, each mineral constituent has its own element composition and particle size distribution, that can be most exactly inferred from elemental and mineralogical composition of physically separated grain-size fractions (Garzanti et al., 2011; von

Eynatten et al., 2016; Li et al., 2020). Such an exact approach would be too laborious or inaccessible in reality, especially in cemented and consolidated sediments. The impossibility to apply an exact approach leaves space for a "proxy approach" and empirical data processing, such as plotting weathering proxies against grain-size proxies, such as Al/Si or Zr/Rb (Lupker et al., 2013; Guo et al., 2018; Deng et al., 2019; Matys Grygar et al., 2019b; Bosq et al., 2020) and evaluation of the resulting patterns. Real grain-size correction of weathering indices has not been proposed up to now, except for K/Si ratio with grain-size effect compensated by linear regression with Al/Si (Lupker et al., 2013). The weathering proxy such as a corrected K/Si ratio can be considered a departure (residual) of K/Si in the sediment composition scatterplot, which closely resembles extraction of chemical contamination signal as departure of grain-size control scatter plots in environmental geochemistry (Matys Grygar and Popelka, 2016).

Empirical data processing requires empirical evaluation of their performance. The most straightforward way is to examine their beneficial role in typical tasks of the sedimentary geochemistry, such as improvement of lateral correlation of core logs, decreasing "noise", i.e. inter-sample scatter due to possible diagenetic alterations or other anomalies, and separation of useful desired geochemical signal. Such tests by "real performance" are more persuading than formal statistical criteria, which can only be derived from the adopted mathematical models, not from real fidelity in approaching natural complexity. Any compositional data treatment should primarily answer geoscientific questions.

Orbital signatures are particularly important signals and information in integrated stratigraphy and palaeoclimate studies (e.g., Hilgen et al., 2012; Martinez et al., 2015; Kochhann et al., 2016; Beddow et al., 2018; Meyers, 2019). Statistical tests based on power spectra are not always sufficient to confirm the unequivocal presence of orbital signals, as demonstrated by the identification of "false positives" (e.g., Vaughan et al., 2011). Other tests should also be applied, as there are many hindrances that prevent sediments from recording orbital cycles unequivocally (Schwarzacher, 2000). The environment in sedimentary basins is rarely uniform, particularly in continental settings with

dynamic catchment topography and hydrological regime. Autogenic processes or autocycles, which commonly shape fluvial, deltaic, and lacustrine systems by alternating lateral and vertical deposition patterns and sediment reworking (Schwarzacher, 2000), influence sediment grain-size and thus their chemical composition and contaminate the climatic signal in sediments *sensu* Meyers (2019). Lateral correlation of sediment profiles is conventionally required to interpret sedimentary basin fills without the interference of autogenic processes (e.g., Uličný et al., 2009). Similarly, true orbital (climatic) signals should be tested for lateral stability and independence of sediment lithology (Ait-Itto et al., 2018; Matys Grygar, 2019; Weedon et al., 2019).

Compositional data processing should respect their mathematical (e.g., Tolosana-Delgado and von Eynatten, 2010; Pawlowsky-Glahn et al., 2015) and physico-chemical specifications (Matys Grygar and Popelka, 2016), which hinder the use of raw concentrations or plain concentration ratios in interpreting chemical composition. Raw compositional datasets commonly do not show a Gaussian (normal) distribution, but more importantly, their direct processing ignores the fact that the relevant information in compositions is contained in log-ratios. The common real-space representation of compositional data is calculated from the family of orthonormal isometric log-ratio (ilr) coordinates (Tolosana-Delgado and von Eynatten, 2010; Pawlowsky-Glahn et al., 2015). The system of pivot coordinates also belongs to that family (Filzmoser et al., 2018), and is used here. As in real observations, abundant extreme values can naturally occur in compositional data. They are sometimes considered as outliers and their influence should be suppressed in a way that it does not impact the spectral analyses (e.g., Weedon, 2003). Robust regression (RR) should be preferred to the ordinary least-squares method in geochemical analyses, which has yet to be recognised for the environmental geochemistry of sediments (Matys Grygar and Popelka, 2016; Birch, 2017). Although robust statistics have already been established in the context of compositional data (Tolosana-Delgado and McKinley, 2016; Filzmoser et al., 2018), the implementation of robust approaches in sedimentary geochemistry is still rare (Fačevicová et al., 2016).

Sediment records in the Miocene Most Basin, the Czech Republic, formed just before and in the early stages of the Miocene Climatic Optimum (MCO) (Rajchl et al., 2009; Matys Grygar et al., 2014, 2017a, 2017b, 2019a), and are used hereafter to make a progress in the use of chemical weathering proxies. This study respects the known mathematical specificity of compositional data. Besides previously tested K/Al and K/Ti ratios (Matys Grygar et al., 2019b), we hereafter refine K/Al, Mg/Al, and K/Rb ratios. Enrichment factors, one of the conventional tools for processing compositional data in environmental geochemistry (Jung et al., 2014; Matys Grygar and Popelka, 2016; Birch, 2017), and robust regression residuals (RRes) (Maronna et al., 2006) are applied to achieve the desired corrections. Several element ratios have already been used as chemical weathering proxies, e.g., Al/K or K/Al (Garzanti et al., 2013; Hu et al., 2013), K/Si (Lupker et al., 2013), Rb/K or K/Rb (Buggle et al., 2011; Hu et al., 2013; Profe et al. 2016; Bosq et al., 2020), K/Ti (Arnaud et al., 2012; Degeai et al. 2018), and Al/Mg (Dinis et al., 2017). Their grain-size control has not been fully compensated, except for K/Si (Lupker et al., 2013). Compared to our preceding study on improvement in the use of K/Al and K/Ti ratios as palaeoclimate proxies from mineralogical and geochemical points of view (Matys Grygar et al., 2019b), this novel study extends the number of weathering proxies and employs a RR with isometric log-ratio (ilr) coordinates of the selected element sub-compositions as explanatory variables to fully respect the mathematical-statistical properties of geochemical datasets (Buccianti et al., 2006; Bloemsma et al., 2012; Reimann et al., 2012; Flood et al., 2016).

2 Geological setting

The geological map of the Most Basin is shown in Fig. 1. The basin floor subsidence started in the Oligocene by mafic volcanic effusions in the České Středohoří and Doupov mountains (Rajchl et al., 2009; Mach et al., 2014). The Most Basin sediments were formed by weathering products of mafic volcanic rocks SW and NE of the basin floor, Cretaceous marls or limestones E of the basin, and Palaeozoic sediments and crystalline rocks of Bohemian Massif S of the basin (Fig. 1). The source rocks were subjected to weathering under a climate more humid and warmer than the present-day

Mid European temperate climate (Kvaček and Teodoridis, 2007; Matys Grygar et al., 2019b). The major rivers flowed to the basin from the S and SE. The basin was hydrologically open. In early Miocene the entire basin floor was covered by peat swamp and alluvial plains, which lead to accumulation of organic matter and subsequent formation of the Main Coal Seam still exploited. The peat swamp then developed to the basin wide lake with clastic deposits, which are subject of this study. The contribution of local mafic volcanic rocks to studied sediments was minor (Mach et al., 2014; Matys Grygar et al., 2019b).

The stratigraphy of the Most Basin fill has been described by Rajchl et al. (2009), Mach et al. (2014), and Matys Grygar et al. (2017a). The age of the studied sediments was delimited by biostratigraphy (Kvaček and Teodoridis, 2007) and refined by cyclo- and magnetostratigraphy (Matys Grygar et al., 2019a). The studied lacustrine sediments of the Most Basin are monotonous greyish to brownish clay-silt mixtures (Matys Grygar et al., 2014, 2017). The X-ray diffraction analysis of these sediments showed major clay minerals illite-smectite, kaolinite, quartz, siderite, and minor K-feldspars and pyrite (Matys Grygar et al., 2017a). The sediments are so monotonous that only chemostratigraphy can produce correlation framework for the basin (Matys Grygar et al., 2014, 2017a, 2019a).

3 Methods

3.1 Sampling and analyses

The studied drill cores (Table A.1) were obtained in the frame of the Czech state project VODAMIN, led by Palivový kombinát s.p. (Fuel Combinate) in Ústí nad Labem (DU7, HK930) and by North Bohemian Mines, j.s.c., Bílina (DO565). The lithological description and stratigraphic evaluation of the cores have been provided by the North Bohemian Mines. Details of sampling and sample processing (air drying, grinding with planetary mill) have been described previously (Matys Grygar et al., 2017a, 2019a).

Chemical analyses were performed with an X-ray fluorescence (XRF) spectrometry large-area Si drift detector using an Epsilon 3^X instrument (PANalytical, the Netherlands) as described previously

(Matys Grygar et al., 2017a, 2019a). Micro-milled samples were analysed as powder in nylon cells with Mylar foil bottoms. The intensities of the analytical signal were optimised for selected elements from Mg to Rb and calibrated using certified reference materials. The XRF results are mostly presented as element ratios, which are more robust from the point of view of the XRF methodology (Grützner and Higgins, 2010; Flood et al., 2016).

The magnetic polarity was obtained conventionally with a 755 4K SRM (superconducting rock magnetometer, William S. Goree, Inc., Sand City, CA) after stepwise alternating field demagnetisation, as reported previously (Matys Grygar et al., 2017a, 2019a). Individual samples (several samples per core) with polarity opposite than their neighbours were discarded from the interpretation. Polarity reversals identified in studied cores are listed in Table A.2, and an inclination depth profile for HK930 is depicted in Fig. A.1.

3.2 Data processing

Local enrichment factors (LEFs) were calculated by ordinary regression using MS Excel (Microsoft) or Origin (OriginLab Co., Northampton, MA). The principle of LEFs is depicted in Fig. A.2. LEFs were calculated for the K/Al, Mg/Al, and K/Rb element ratios using Al/Si, Zr/Rb, Ca, and/or Fe as independent variables. Al, Si, Rb, and Zr, in particular their ratios Al/Si and Zr/Rb are broadly applicable grain-size proxies (Chen et al., 2006; Bouchez et al., 2011; Lupker et al., 2011, 2013; Flood et al., 2016; Matys Grygar and Popelka, 2016; Thöle et al., 2019), although both Al/Si and Zr/Rb can also be influenced by sediment mineralogy and provenance (Profe et al., 2016). The principle of LEF in this study is the same as that of the enrichment factor EF of local EF (LEF) in environmental geochemistry (Matys Grygar and Popelka, 2016; Birch, 2017): the target element ratio is divided by the ratio calculated from a baseline function for the target sample using a suitable independent (explanatory) variable.

In order to reveal the relationship between the eccentricity and the given element (log-)ratios, the effect of mineralogy and grain size has been corrected prior to the analysis. This correction has been

performed through the regression model with the analysed (log-)ratio as dependent variable. Since the data in hand and consequently also the results of the analysis can be affected by the presence of some atypical values (outliers), the robust approach, in particular so-called MM-estimates of the regression parameters, was used (Yohai, 1987; Koller and Stahel, 2011). At the side of regressors (explanatory variables), the grain size was represented by the Zr/Rb (log-)ratio and mineralogy by the ilr transformed subset of elements, typically Al, Fe, Ca and Mg (Pawlowsky-Glahn et al., 2015). Mg was excluded from that subset for Mg/Al at the dependent variable side. For further analysis of the orbital signal, RRes were used. The computations were carried out in the R software environment (R Core Team, 2019); for the RR the function lmrob from package robustbase (Maechler et al., 2019) was employed.

Spectral analyses in the depth domain were performed as described previously (Matys Grygar et al., 2017b). Where necessary, the datasets were detrended to make the mean and the variance of the analysed signal stationary. The spectral analyses were then carried out using the multi-taper method with three 2π-tapers (Thomson, 1982, 1990). The confidence levels were calculated using the Mann and Lees (1996) method modified in Meyers (2014). Taner filters were then used to isolate frequency bands of interest in the spectra as specified in Prokopenko et al. (2006). Analysis in the time domain using 'testPrecession' (Zeeden et al., 2015) was performed to validate the presence of precession signals and their related eccentricity amplitudes in magnetic polarity timescales and eccentricity-matched depth-age models as in Matys Grygar et al. (2019a).

3.3 Depth-age models

The chemostratigraphic scheme and age models for the Most Basin sediments (Matys Grygar et al., 2014, 2017a, 2017b, 2019a) include lateral correlation of geochemical depth profiles, association of diagnostic features in K/Al and K/Ti to orbital signals according to the astronomical solution (Laskar et al., 2004), and magnetic polarity analysis and assignment of the magnetic polarity zones to polarity chrons. Initial age models for the drill cores were obtained by magnetic polarity analysis (Matys

Grygar et al., 2017a, 2017b, 2019a) with polarity time scales derived from ATNTS2012 (Hilgen et al., 2012) and/or Kochhann et al. (2016), and then refined by matching K/Al or K/Ti minima to the eccentricity maxima as described by Matys Grygar et al. (2019a). Ages of the polarity reversals identified in the studied cores are listed in Table A.2. Fig. A.3 documents the development of the depth-age model for core HK930: the K/Ti depth profile with prominent minima K1 to K5 (Fig. A.3A), their misfit when ATNTS2012 polarity time scale was adopted (Fig. A.3B), and finally a match to the temporally nearest eccentricity maxima (Fig. A.3C).

The 'testPrecession' algorithm (Zeeden et al., 2015) was used to show the probability of the null hypothesis of precession forcing by combining the polarity time scales of ATNTS2012 (Hilgen et al., 2012) and Kochhann et al. (2016) and eccentricity-matched depth/age models (Table A.3 for HK930 core). In the same way, as in Matys Grygar et al. (2019a), the combination of polarity time scales and individual eccentricity matching age models provided the best results. In this paper, we employed the same procedure for cores HK930, DU7, and DO565. The depth-age model for core HK930 showed that 192 m of sediments above the Main Coal Seam were deposited within ~850 ky, which represents a mean deposition rate of 23 cm ky^{-1}.

4 Results

4.1 Local enrichment factors (LEFs)

The K/Al ratio in the Most Basin sediments was found to be partly controlled by the sediment grain size (Fig. A.2). The grain-size influence, as well as the influence of autochthonous carbonates, were corrected by conversion of the raw K/Al ratio to its LEF defined as

$$LEF = (K/Al)/(K/Al)_{base}$$

where $(K/Al)_{base}$ was calculated by linear regression of K/Al with Al/Si and in one case with Al/Si and Fe concentration (actual variables for individual cores are listed in Table 1) as independent (explanatory) variables. The principle of LEF calculation is shown in Fig. A.2 for a single explanatory variable. The definition of LEF resembles that of α^{Al} proposed by Garzanti et al. (2013)

$\alpha^{Al}_{K} = (Al/K)/(Al/K)_{UCC}$

where UCC is the mean upper continental crust. LEF differs from α^{Al} by replacing the global reference (UCC) by using a local background function for K/Al, which is not pre-defined but is found as multilinear regression function individually for each drill core. Lithologically corrected and raw K/Al has the largest correlation coefficients among pairs of raw and LEF element ratios (Table A.4), showing that the K/Al ratio has the lowest grain-size influence.

The K/Si ratio was also tested as a proxy. Aluminium and silicon have actually opposite relationships regarding sediment grain size, but both normalising elements correct the raw K concentrations for the variable siderite content in the studied sediments, because both Al and Si are equally diluted by siderite present in sediments in variable proportions (Matys Grygar et al., 2017a). The performance of the grain-size correction of K/Si is shown in Fig. 2, B. The efficiency of the grain-size corrections of K/Al and K/Si using background functions is documented by the largest pair correlation of all proxies examined in this work: K/Al LEF and K/Si LEF (Table A.4). The depth profiles of K/Al LEF and K/Si LEF are also similar (Fig. 3). The correction of K/Si grain size dependence by linear regression with Al/Si was also used successfully by Lupker et al. (2013).

The Mg/Al ratio in sediments was partly controlled by the sediment grain size (Al/Si) and to a considerable degree by the presence of carbonates, which was manifested by the Mg/Al dependence on Fe and/or Ca. The Mg/Al LEF was then calculated similarly as K/Al LEF, with $(Mg/Al)_{base}$ calculated using the variables shown in Table 1.

The K/Rb ratio was found to be controlled by Fe concentrations (Fig. 2D), which prevented recognising its orbital signal in the Most Basin sediments during our previous work. The major influence of the siderite content on the K/Rb ratio is documented by the weakest correlation in the pairs of raw and LEF corrected K/Rb (Table A.4). The K/Rb ratio was converted to K/Rb LEF similarly as described above with Fe as an independent variable. The resulting K/Rb LEF does not show control by Fe (Fig. 2E) nor Al/Si (Fig. 2F).

4.2 Robust regression on log-ratios

RR performed on log-ratios at both response and explanatory sides was tested for the same purpose as LEF, i.e., for the correction of weathering proxies for grain size and carbonate extent, but RR should be better suited for processing compositional data and their relative nature as discussed above. The RR models were applied to the K/Al, K/Si, K/Rb, and Mg/Al ratios, selected according to high values of the robust correlation measure (Rousseeuw and van Driessen, 1999) with the value of eccentricity, inspected on data from DU7 drill core (Fig. A.4). Robust correlation estimates were based on the minimum covariance determinant (MCD) estimator of location and scatter (Rousseeuw and van Driessen, 1999). This robust estimator looks for the subset of the n/2 most consistent observations, and is implemented as the covMcd() function in the R Software. The heatmap (Fig. A.4) highlighted the largest correlation of eccentricity with K/Si ratio.

The explanatory variables for RR are listed in Table 2. Logarithms of (Al/Si) or (Zr/Rb) were used as grain-size proxies. Sub-compositions of elements Si, Fe, and Ca (for Mg/Al), Si, Fe, Ca, and Mg (for K/Al), or Al, Fe, Ca, and Mg (for other element ratios) were used to explain the effect of mineralogy, in particular, of autochthonous carbonates. To respect the relative nature of concentrations, these sub-compositions have been used in the form of ilr coordinates (Filzmoser et al., 2018). The independence of RRes on grain-size proxies was confirmed after each regression. Not all results are shown; only an example of K/Si RRes independence on Al/Si is demonstrated in Fig. 2C.

4.3 Comparison of raw and corrected element ratios in HK930

The correlations between raw and lithologically corrected element ratios are shown in Table A.4 for the HK930 drill core. The correlations between different element ratios are mostly larger for their LEFs than for the raw concentration ratios and are usually lower for their RRes. LEF correction thus seems to *unify* the response of element ratios to the non-lithological (orbital) control, while RRes correction apparently rather *isolates* some specific features of the individual element ratios. This

contrasting behaviour shows distinct natures of LEF and RRes corrections. The unifying character of LEF is demonstrated in Fig. 3.

Fig. 4 shows the comparison of raw element ratios and their lithologically corrected values in the depth profiles of the HK930 drill core. Generally, the main features in the depth profiles are preserved after the lithological corrections. In the case of K/Al in Fig. 4A, the main impact of the corrections is the removal of a long-term decreasing trend, that underpins the short-term variations highlighted by vertical rectangles in the figure.

The raw K/Rb in Fig. 4B shows scatter, which can be suppressed by plotting a 3-point median. The scatter is caused by local (single-point) K/Rb maxima coeval with siderite (Fe concentration) maxima (Fig. 2D) and can be considered as geochemical noise in the depth series. That scatter is efficiently suppressed by using LEF and RRes, which really corrects even the single-point K/Rb maxima. The corrections highlight local variations shown by vertical rectangles in Fig. 4B, most of which are not discernible in the median-smoothed raw K/Rb.

4.4 Depth-age model for studied drill cores

The existing polarity time scales (the reversal dating for the studied time interval is shown in Table A.2) did not produce consistency of sediment geochemistry and astronomical solution, while the combination of those time scales (Matys Grygar et al., 2019a) and even better, the eccentricity-matched age model resulted in a good match between the data and the orbital solution (Table A.3). Spectral analysis and peak-to-peak matching confirmed that the short-eccentricity maxima can be tied to the minima of K/Si (uncorrected ratios) and K/Al (in particular RRes) for the period of 17.7 to 17.05 Ma, i.e., the K1 to K5 minima in Fig. 3 are associated with major eccentricity maxima (Fig. A.3). The eccentricity maximum, centred at 17.391 Ma in La2004 (Laskar et al., 2004) was so weak relative to the other eccentricity maxima that it has no clear counterpart in the geochemistry depth profiles. It may also cause underestimation of total eccentricity cycles and the corresponding total duration of HK930 deposition (estimates based on eccentricity counts are shortest in Table A.5). The dominant

eccentricity signal also completely disappeared in the Most Basin sediment geochemistry at a nearly circular Earth orbit around the eccentricity maximum centred at ca. 17.008 Ma in La2004.

The K2 to K5 minima can be correlated throughout the entire basin (Matys Grygar et al., 2017a, 2017b). The depth-age models for DU7 and DO565 were thus produced by matching K1 to K5 to the same eccentricity maxima as in HK930.

4.5 Spectral analysis in HK930

All four examined element ratios in raw and lithologically-corrected versions (in core HK930) were subject to spectral analysis. The short eccentricity (e) was found at wavelengths at 22-32 m (median 27 m), obliquity (O) at 8-15 m (median 11 m), and precession (P) 3-6 m (main modal maxima 4 and 5 m). The overview is shown in Fig. 5 and Table A.5. These wavelengths are consistent with the results for other time-parallel cores published previously (Matys Grygar et al., 2014, 2017b, 2019a, 2019b). The astronomical solution by Laskar et al. (2004) shows periods of 95, 41, and 21 ky for short eccentricity, obliquity, and precession in the respective time interval. The pairs of wavelengths and cycle durations were used to estimate mean sedimentation rates and the corresponding duration of HK930 deposition (Table A.5). The orbital cycles are notably well expressed on the 2π-MTM spectra of the K/Al and K/Si ratios, both for the raw weight ratios and RRes. It is also observed in the raw K/Rb (but not in K/Rb RRes) and in the Mg/Al RRes (but not in the raw Mg/Al weight ratio). Spectra filtering and evolutive FFT analyses of raw and RRes are shown in Figs. A.5, A.6, A.7. The spectra filtering allowed for estimating total cycle counts in HK930, and thus the total duration of deposition (Table A.5). All the estimates were plausibly consistent.

The raw and lithologically corrected element ratios show variable performance in spectral analysis. Generally, LEF correction slightly weakened orbital signals compared to the corresponding raw element ratios or their RRes. RRes tend to remove long-term trends (Fig. 4), but also somehow suppress the record of the precession cycles, making their counting challenging. Thus, while lithologically corrected element ratios should bear clearer orbital signals regarding their geochemical

nature, it may not always be beneficial for cycle identification by statistical criteria. Obviously, the independent variables used for "cleaning" (grain-size correction) also bear some orbital signal, as demonstrated in Fig. 6. We have already observed that some K minima bear some grain-size components, at least in some portions of the minima, where normalised K concentrations change simultaneously with changes of Al/Si or Zr/Rb (Matys Grygar et al., 2019a).

The Mg/Al ratio shows an eccentricity signal, which is considerably clearer in RRes (Figs. 5, A.5). An obliquity signal is evident in both raw data and LEF, apparently stronger in some specific depth intervals, particularly under low eccentricity, and it is particularly strong in RRes. The precession signal is weak in raw data, and a bit better in RR and even weaker in LEF than in raw Mg/Al. Generally, the precession signal is strong when the obliquity is weak and *vice versa*.

K/Si has a clear eccentricity signal in raw data, while neither LEF nor RRes improved it, showing that K/Si is considerably influenced by the grain-size signal. Obliquity is obvious in raw and RRes-corrected K/Al and K/Si, but it is less clear in their LEFs. Precession was better observed in raw K/Rb and Mg/Al. For K/Rb (Fig. A.7), RRes extend the depth interval with the eccentricity signal, and both LEF and RR enhance the power of the eccentricity signal. The obliquity signal is better in LEF and worse in raw data. The strongest precession signal is in raw K/Rb and both corrections suppress it, perhaps because the Fe concentration, used for the K/Rb lithological corrections, bears an orbital signal as well (Fig. 6). Generally, K/Rb shows the strongest precession signal of all proxies, which could be favourable for orbital tuning. LEF and RR decrease the noise in the power spectra by correcting the Fe-controlled "outliers", but are not essential for orbital signal isolation by spectral analysis. A weakening of the precession signal due to lithological corrections was also found by 'testPrecession' (Table A.3), but it was mostly caused by the non-linear response of K/Rb to the precession forcing (Fig. A.8).

In the K/Al ratios (Fig. A.6), the eccentricity shows the largest power relative to noise in raw data and in RRes. The same is valid for obliquity. Precession is a bit variable in individual proxies, but generally, no data treatment is markedly better than others. The powers of precession and obliquity are

commonly similar, which could hinder the use of those signals for orbital tuning by the manual match of geochemistry and calculated orbital parameters.

4.6 Lateral correlation of weathering proxies

The most reliable way to evaluate possible provenance control or topography-related effects should be to compare records from spatially remote cores within the same basin, where the non-climatic controls should weaken the lateral correlation. Because the Most Basin cores are aligned by their K1 to K5 minima in K/Al or K/Ti logs, the lateral stability of their geochemical depth profiles can be judged from examination of other weathering proxies Mg/Al and K/Rb (Figs. 7, 8). Mg/Al RRes can be considered mineralogically partly independent of K/Al as their values show poor correlation (Table A.4). K/Rb LEFs weakly correlate with K/Al LEFs, but these two proxies show different orbital patterns as shown in section 4.5.

The K/Rb LEF shows a weak expression of short eccentricity in DU7 and HK930, and thus K1 to K3-related minima cannot be clearly discerned in DU7 (Fig. 7). The major feature of K/Rb LEF is the high power of precession signal revealed by spectral analysis of HK930 (Fig. 5), although this signal has a variable amplitude (sensitivity to forcing), which weakens its manifestation according to 'testPrecession' (Table A.3). The clear precession control results in the possibility of practically peak-to-peak correlation of K/Rb LEF minima highlighted by black vertical lines in Fig. 7 in the area of K3 to K5 between individual cores and with actual precession maxima in the astronomical solution. The inter-core discrepancies in some maxima could be adjusted by minor precession tuning, which is, however, not the aim of this work.

The Mg/Al shows obliquity-controlled variability (Fig. A.5), which is highlighted by black rectangles in Fig. 8. Similarly, as in the case of K/Rb, the inter-core correlation is obvious in the area from K3 to the top of the core. Both K/Rb and Mg/Al thus show a plausible lateral stability at the basin-scale level. Lithologically-corrected Mg/Al ratios, particularly RRes, have a strong power of obliquity (Figs. 5, A.5)

and the examined cores show plausible lateral correlation of Mg/Al minima with obliquity maxima according to the astronomical solution (black rectangles in Fig. 8).

The lithogenic corrections cannot exclude inherent physical uncertainties in the interpretation of weathering intensities recorded in sediments, in particular basin topography (Garzanti et al., 2013; von Eynatten et al., 2016; Joo et al., 2018) and provenance (von Eynatten et al., 2016), which give weathering indices only relative (site- and time-specific) values. We attribute certain lateral differences between DO565, DU7, and HK930 cores to site-specific topography and provenance effects. The inter-core differences are particularly pronounced in K/Rb (Fig. 7), where some minima are clearly site-specific.

5 Discussion

5.1 Lithological correction of weathering proxies

It has been common in sedimentary geochemistry to work with weathering proxies according to the original definitions, like the chemical index of alteration (CIA) (Nesbitt and Young, 1982) not corrected for lithological control. The original CIA definitions include a sum of Ca, Na, and K ions as mobile cations:

$$CIA = [Al_2O_3/(Al_2O_3+CaO^*+Na_2O + K_2O)] \times 100$$

where CaO* corresponds to non-carbonate Ca. The CIA grain-size control is complicated by element-specificity of grain-size control of each of those mobile elements (Bouchez et al., 2011; Garzanti et al., 2011; Bloemsma et al., 2012; von Eynatten et al., 2016; Pang et al., 2018). The α^{Al}_{M} indices by Garzanti et al. (2013) (section 3.1), where M stands for mobile ions, are an example of simple geochemical normalisations, which partly correct K variations from grain-size control due to the similar particle size of K and Al carriers in at least moderately mature sediments. However, *similar* is not *equal* and the simple normalisation may cause minor, but systematic trends of the element ratios with changing sediment grain size. In environmental geochemistry, such a systematic bias has been called “secondary grain-size effect” (Jung et al., 2014; Sun et al., 2018a). The low attention to real

grain-size corrections of weathering indices in published studies is surprising, because the grain-size control of the mobile ion concentrations is known (see Introduction) and simultaneously (at least) two grain size proxies broadly applicable to geochemically mature sediments with non-changing provenance are readily available: Al/Si and Zr/Rb (Chen et al., 2006; Bouchez et al., 2011; Matys Grygar and Popelka, 2016; Profe et al., 2016; Pang et al., 2018; Hatano et al., 2019; Thöle et al., 2019). Both LEFs and RRes in this work employed those proxies to perform lithological corrections (Tables 1, 2).

In the Most Basin, the concentrations of mobile elements K and Mg have also been affected by autochthonous carbonates, in particular, siderite. The phenomenon has not yet been addressed in processing the K- and Mg-based weathering proxies. There are two distinct consequences of the carbonate presence: direct (stoichiometric) and indirect (diagenetic). The stoichiometric effect in the Most Basin proxies concerns Mg, which partly substitutes Fe in siderite as it is common in lacustrine siderites (Lojka et al., 2009). Similarly, if the Ca concentration is included in weathering indices such as CIA, its content in diagenetic carbonates must be subtracted, as conventionally performed by acid leaching before the element analysis (Nesbitt and Young, 1982). We would not recommend the acid leaching for siderite-cemented clays for two reasons: (1) siderite removal would require more concentrated acids than calcite, and they would etch clay minerals including K- and Mg-bearing illites and smectites; and (2) the chemical treatment would make sample processing more demanding and less environmentally friendly compared to simple mathematical correction of the compositional data.

The performance of K/Rb as a climate proxy is based on the stronger retention (slower liberation) of heavier alkaline metal ions from clay minerals relative to lighter alkaline metal ions (Wampler et al., 2012; Garzanti et al., 2013; Tanaka and Watanabe, 2015; Bosq et al., 2020). Apparently, the K/Rb ratio should be an ideal proxy for higher chemical weathering intensities, which passed to the level of aging and partial dissolution of clay minerals. In the Most Basin, the K/Rb ratio was partly controlled by Fe concentrations (Fig. 2), which we attribute to an indirect (diagenetic) impact of the siderite crystallisation. We do not have any explanation for this control, however, re-crystallisation of clay

mineral grains around the autochthonous siderite crystals has been reported by Geptner et al. (2016) and attributed to bacterial activity. The sensitivity of the K/Rb ratio to sediment diagenesis has been reported by van de Kamp (2016). Irrespective of what process is behind this influence, the K/Rb ratio in the Most Basin sediments needs chemical corrections, for which concentrations of Fe (Table 1) or Fe, Ca, and Mg (Table 2) were used. The possible effect of carbonates in sediment geochemistry should thus be checked if weathering proxies are used even in the case the evaluated cations are not constituents of the carbonates, that could not be expected in advance.

The lithological "cleaning" (corrections) of weathering proxies may not be beneficial for all purposes of compositional data processing. The spectral analysis of the Most Basin sediments also yielded useful results using the (grain-size) uncorrected K/Ti (Matys Grygar et al., 2014) or K/Al ratios (Matys Grygar et al., 2017a). The sediment lithology may also reflect the palaeoclimate by other mechanisms than chemical maturation of the catchment soils, in particular, catchment erosion and hydrological sorting before sediment deposition. The orbital control of the Most Basin sediment lithology is obvious from the orbital signal in (uncorrected) lithological proxies (Fig. 6). The performance of the uncorrected K/Ti ratio can further be attributed to the fact that it is easily obtained at good quality by XRF analysis as K and Ti has very close energies of analytical signals and thus similar disturbances by spectral interferences and matrix effects (e.g., Grützner and Higgins, 2010; Thöle et al., 2019). In this study, we avoided the K/Ti element ratio because the Ti concentration in sediments showed a provenance control in the Ohře Rift (Matys Grygar et al., 2016, 2017a). On the other hand, both changes in provenance (e.g., switching between sediment yield in geologically distinct catchments) and lithology can bear climatic signals in a particular sedimentary basin, e.g., due to precipitation-controlled fluvial activity and the ratio between chemical and physical erosion in the tributary river systems. The cleaning of the orbital signal is hence not indispensable for local lateral correlations or for construction of age models using cyclostratigraphy, if the climate-recording mechanism is not addressed. The orbital signatures in raw element ratios in the Most Basin are mostly stronger than after their lithological correction (Fig. 5, Table A.3). On the other hand, if the lithological correction is

performed, the variations in weathering proxies can be unequivocally assigned to weathering intensity and not to other controlling factors.

5.2 Consequences for palaeoclimate research

Compared to the existing late Oligocene and early Miocene marine sediments, the composition of which is usually mainly controlled by eccentricity (Kochhann et al., 2016; Liebrand et al., 2016), the Most Basin is exceptional also by showing short eccentricity, obliquity, and precession cycles, with the power of individual signals specific to individual weathering proxies (Fig. 5). The expression of all those three main short orbital cycles is extraordinary, also because a prevalent part of the Miocene sedimentary archives has a lower temporal evolution. Refining separation of orbital signals by choice of suitable element proxies can be valuable to understand palaeoclimate dynamics. The obliquity signal in the Most Basin might seem surprising to be pronounced in the mid-latitudes of Europe, far from high latitudes, but explanations have been proposed even for tropical regions, even without the assumption of long-range control of tropics by high latitude areas (Bosmans et al., 2015; Ochoa et al., 2018). The refinement of weathering proxies can thus bring progress in future studies of global climate dynamics.

The power of the eccentricity, obliquity, and precession signals has already been found specific to individual proxies and stratigraphic levels in the Most Basin (Matys Grygar et al., 2014, 2017b, 2019b) but it is considerably improved in this study. The variable relative powers of eccentricity, precession, and obliquity are also known and discussed in other records of sufficient duration and temporal resolution (e.g., Boulila et al., 2015; Herb et al., 2015; Martinez et al., 2015; Marshall et al., 2017). It may be attributed to low-eccentricity periods (eccentricity nods) and a variable sensitivity of the Earth climate to individual forcing mechanisms; both those aspects are relevant in sedimentary geochemistry studies. The first situation may be predicted from the astronomical solution (Laskar et al., 2004) and it may be used to confirm the correctness of the depth-age models by identification of the eccentricity nodes, such as that around 17.0 Ma (Matys Grygar et al., 2014), or low amplitude

eccentricity cycles at ~17.4 Ma with a missing expected K minimum (between K2 and K3, as discussed above). The second situation is less trivial and may be attributed to reconstructions of global climate mechanisms, such as variable dynamics of polar ice sheets depending on their extent and position. Variable climate sensitivity can be directly observed in sedimentary records, as in the case of the Early-to-Middle Pleistocene transition at ca. 1.0 Ma, when glaciation control switched from obliquity to eccentricity (e.g., Herb et al., 2015). The Most Basin record showed a weakening of the eccentricity control in favour of obliquity control after the onset of the MCO, i.e., after 17.0 Ma (Figs. A.6, A.7), although the orbital eccentricity was not persistently low in that time period. We interpret this as a change in the dynamics of the Earth´s climate system due to the shrinking of the Antarctic Ice Sheet and the faster response of smaller ice bodies to orbital forcing (De Vleeschouwer et al., 2017).

The findings in the Most Basin can be relevant for the study of marine palaeoenvironmental archives of the late Oligocene to early Miocene (Kochhann et al., 2016; Liebrand et al., 2016; Miller et al., 2017). The marine records, mostly employing stable carbon and oxygen isotopes in biogenic carbonates, are dominated by eccentricity signals with weak and variable power of obliquity (Liebrand et al., 2016). The dominance of the eccentricity signal in marine sediments of the late Oligocene and early Miocene was found by Kochhann et al. (2016), Liebrand et al. (2016), and Beddow et al. (2018) and it was proposed as the major signal for the orbital tuning of their age models. In the period around the MCO onset at ca. 17.0 Ma and soon after that, a weakening of the eccentricity signal is observed in the Most Basin weathering record. If that change represented a change of the global Earth's climate system, the orbital tuning to eccentricity might be an issue in marine sediments. Indeed, the actual dating of the abrupt $\delta^{18}O$ shift associated with the MCO onset coeval with the abrupt decrease in chemical weathering proxies (intensification of chemical weathering) (Fig. 4) near 17.0 Ma in the Most Basin (Matys Grygar et al., 2017b, 2019a; this study) is currently not consensual. Miller et al. (2017) critically discussed the results of Kochhann et al. (2016) and denied their age model and timing of the MCO onset. Studies of the MCO onset would

undoubtedly require sedimentary records with precession-scale resolution and as much detailed orbital signatures as possible to produce a robust age model. However, the detection of obliquity cycles may be controversial in some marine sediments, as discussed in Liebrand et al. (2016).

The unequivocal isolation of individual orbital signals in siliciclastic sediments of continental origin could help bridge the current gap between continental and marine (mostly biogenic) palaeoclimatic records and contribute to the verification of marine records discussed above. Lithological contamination of palaeoclimatic signals is probably the major challenge for most fluvial, lacustrine, and estuarine sedimentary records from a purely geochemical point of view. This study could pave a road to a progress in this direction.

6 Conclusions

Corrections of weathering proxies, based on concentration ratios of mobile (K and Mg) and conservative elements (Al, Rb, Si), are needed in order to separate the palaeoclimate information. Lithological corrections include grain-size control and the influence of the diagenetic formation of carbonates, the latter being particularly important for the Mg/Al and K/Rb ratios in the studied sediments. These corrections can be achieved by ordinary regression in a concept of local enrichment factors and RR in the concept of isometric log-ratios. Both raw and lithologically corrected K/Al, K/Si, K/Rb, and Mg/Al ratios carry orbital signals in the lacustrine sediments of the Most Basin. The spectral power of eccentricity, obliquity, and precession are specific to the individual tested element ratios, but also varied in the Most Basin stratigraphy, which we interpret as evidence for the change of the Earth's climate dynamics after the onset of the Miocene Climatic Optimum. The results of the Most Basin sediment analysis show that the sediment grain size itself can carry orbital signals and so, in some cases, the removal of their influence can even weaken the orbital signal in the weathering proxies; that weakening proves certain non-climatic contamination of the uncorrected weathering proxies.

Acknowledgment

The DO565 core was kindly provided by the North Bohemian Mines, j.s.c., Bílina, and cores DU7 and HK930 by Palivový kombinát Ústí, a state enterprise and the VODAMIN project. Funding of research was provided by the Czech Science Foundation, in particular sampling (DO565, DU7, HK930) and XRF and CEC analyses (DO565, DU7) by project 16-00800S. The XRF and CEC analyses (HK930), the entire data processing, and paper writing were supported by project 19-01768S. Sampling was kindly performed by P. Vorm, M. Hošek, and M. Faměra, laboratory sample processing and analyses by M. Maříková and P. Vorm (all Institute of Inorganic Chemistry). TMG thanks J. Grmela (alumni of Mendel University, Brno) for smoked hop addition. The authors appreciate careful work by two anonymous reviewers and the journal chief editor C. Chagué for numerous corrections and improvements of the text.

Data availability

Dataset for HK591 drill core is available for this paper.

Appendix

Part of results is presented in appended document.

References

Ait-Itto, F.-Z., Martinez, M., Price, G.D., Ait Addi A., 2018. Synchronization of the astronomical time scales in the Early Toarcian: A link between anoxia, carbon-cycle perturbation, mass extinction and volcanism. Earth Planet. Sci. Lett. 493, 1–11.

Andreani, L., Stanek, K.P., Gloaguen, R., Krentz, O., Domínguez-González, L., 2014. DEM-based analysis of interactions between tectonics and landscapes in the Ore Mountains and Eger Rift (East Germany and NW Czech Republic). Remote Sens. 6, 7971–8001.

Arnaud, F., Révillon, S., Debret, M., Revel, M., Chapron, E., Jacob, J., Giguet-Covex, C., Poulenard, J., Magny, M., 2012. Lake Bourget regional erosion patterns reconstruction reveals Holocene NW European Alps soil evolution and paleohydrology. Quat. Sci. Rev. 51, 81–92.

Beddow, H.M., Liebrand, D., Wilson, D.S., Hilgen F.J., Sluijs, A., Wade, B.S., Lourens L.J., 2018. Astronomical tunings of the Oligocene–Miocene transition from Pacific Ocean Site U1334 and implications for the carbon cycle. Clim. Past 14, 255–270.

Birch, G.F., 2017. Determination of sediment metal background concentrations and enrichment in marine environments – A critical review. Sci. Tot. Environ. 580, 813–831.

Bloemsma, M.R., Zabel, M., Stuut, J.B.W., Tjallingii, R., Collins, J.A., Weltje, G.J., 2012. Modelling the joint variability of grain size and chemical composition in sediments. Sediment. Geol. 280, 135–148.

Bosmans, J.H.C., Hilgen, F. J., Tuenter, E., Lourens, L. J., 2015. Obliquity forcing of low-latitude climate. Clim. Past 11, 1335–1346.

Bosq, M., Bertran, P., Degeai, J.-P., Queffelec, A., Moine, O., 2020. Geochemical signature of sources, recycling and weathering in the Last Glacial loess from the Rhône Valley (southeast France) and comparison with other European regions. Aeolian Res. 42, 100561. DOI: 10.1016/j.aeolia.2019.100561.

Bouchez, J., Gaillardet, J., France-Lanord, C., Maurice, L., Dutra-Maia, P., 2011. Grain size control of river suspended sediment geochemistry: Clues from Amazon River depth profiles. Geochem. Geophys. Geosyst. 12, Q03008. DOI: 10.1029/2010GC003380.

Boulila, S., Charbonnier, G., Galbrun, B., Gardin, S., 2015. Climatic precession is the main driver of Early Cretaceous sedimentation in the Vocontian Basin (France): Evidence from the Valanginian Orpierre succession. Sediment. Geol. 324, 1–11.

Buccianti, A., Mateu-Figueras, G., Pawlowsky-Glahn, V. (Eds.), 2006. Compositional Data Analysis in the Geosciences: From Theory to Practice. Geological Society, London, special publication 264. DOI: 10.1144/GSL.SP.2006.26.

Buggle, B., Glaser, B., Hambach, U., Gerasimenko, N., Marković, S., 2011. An evaluation of geochemical weathering indices in loess–paleosol studies. Quat. Internat. 240, 12–21.

Chen, J., Chen, Y., Liu, L.-W., Ji, J.-F., Balsam, W., Sun, Y.B., Lu, H.Y., 2006. Zr/Rb ratio in the Chinese loess sequences and its implication for changes in the East Asian winter monsoon strength. Geochim. Cosmochim. Acta 70, 1471–1482.

De Vleeschouwer, D., Vahlenkamp, M., Crucifix, M., Pälike, H., 2017. Alternating Southern and Northern Hemisphere climate response to astronomical forcing during the past 35 m.y. Geology 45, 375–378.

Degeai, J.-P., Villa, V., Chaussé, C., Pereira, A., Nomade, S., Aureli, D., Pagli, M., Nicoud, E., 2018. Chemical weathering of palaeosols from the Lower Palaeolithic site of Valle Giumentina, central Italy. Quat. Sci. Rev. 183, 88-109.

Deng, T., Li, Y., Wang, Z.-J., Yu, Q., Dong, S.-L., Yan, L., Hu, W.-C., Chen, B., 2019. Geochemical characteristics and organic matter enrichment mechanism of black shale in the Upper Triassic Xujiahe Formation in the Sichuan basin: Implications for paleoweathering, provenance and tectonic setting. Mar. Petrol. Geol. 109, 698–716.

Dinis, P., Garzanti, E., Vermeesch, P., Huvi, J., 2017. Climatic zonation and weathering control on sediment composition (Angola). Chem. Geol. 467, 110–121.

Fačevicová, K., Bábek, O., Hron, K., Kumpan, T., 2016. Element chemostratigraphy of the Devonian/Carboniferous boundary – A compositional approach. Appl. Geochem. 75, 211-221.

Filzmoser, P., Hron, K., Templ, M., 2018. Applied Compositional Data Analysis: With Worked Examples in R. Springer Nature Switzerland, ISBN 978-3-319-96422-5.

Flood, R.P., Bloemsma, M.R., Weltje, G.J., Barr, I.D., O'Rourke, S.M., Turner, J.N., Orford, J.D., 2016. Compositional data analysis of Holocene sediments from the West Bengal Sundarbans, India: Geochemical proxies for grain-size variability in a delta environment. Appl. Geochem. 75, 222–235.

Journal Pre-proof

Garzanti, E., Andò, S., France-Lanord, C., Censi, P., Vignola, P., Galy, V., Lupker, M., 2011. Mineralogical and chemical variability of fluvial sediments 2. Suspended-load silt (Ganga-Brahmaputra, Bangladesh). Earth Planet. Sci. Lett. 302, 107-120.

Garzanti, E., Padoan, M., Setti, M., Najman, Y., Peruta, L., Villa, I.M., 2013. Weathering geochemistry and Sr-Nd fingerprints of equatorial upper Nile and Congo muds, Geochem. Geophys. Geosyst. 14, 292–316.

Geptner, A. R., Petrova, V. V., Pha, P.D., Huyen, N.X., Nginh, L.T., 2016. Siderite layers in the fresh-water Neogene sediments of Vietnam. Lithol. Miner. Res. 51, 136–151.

Grützner, J., Higgins, S. M., 2010. Threshold behavior of millennial scale variability in deep water hydrography inferred from a 1.1 Ma long record of sediment provenance at the southern Gardar Drift. Paleoceanography 25, PA4204. DOI: 10.1029/2009PA001873.

Guo, Y.L., Yang, S.Y., Su, N., Li, C., Yin, P., Wang, Z.B., 2018. Revisiting the effects of hydrodynamic sorting and sedimentary recycling on chemical weathering indices. Geochim. Cosmochim. Acta 227, 48-63.

Hatano, N., Yoshida, K., Sasao, E., 2019. Effects of grain size on the chemical weathering index: A case study of Cheek for Neogene fluvial sediments in southwest Japan. Sediment. Geol. 386, 1–8.

Herb, C., Appel, E., Voigt, S., Koutsodendris, A., Pross, J., Zhang, W.L., Fang, X.M., 2015. Orbitally tuned age model for the late Pliocene–Pleistocene lacustrine succession of drill core SG-1 from the western Qaidam Basin (NE Tibetan Plateau). Geophys. J. Internat. 200, 35–51.

Holbourn, A., Kuhnt, W., Kochhann, K.G.D., Andersen, N., Meier, K.J.S., 2015. Global perturbation of the carbon cycle at the onset of the Miocene Climatic Optimum. Geology 43, 123-126.

Hilgen, F.J., Lourens, L.J., Van Dam, J.A., 2012. The Neogene Period. In: Gradstein, F.M., Ogg, J.G., Schmitz, M.D., Ogg, G.M. (Eds.), The Geologic Time Scale 2012. Amsterdam, Elsevier BV, pp. 409-440.

Hu, D.K., Clift, P.D., Boning, P., Hannigan, R., Hillier, S., Blusztajn, J., Wan, S.M., Fuller, D.Q., 2013. Holocene evolution in weathering and erosion patterns in the Pearl River delta. Geochem. Geophys. Geosyst. 14, 2349-2368.

Journal Pre-proof

Joo, Y.J., Elwood Madden, M.E., Soreghan, G.S., 2018. Anomalously low chemical weathering in fluvial sediment of a tropical watershed (Puerto Rico). Geology 46, 691–694.

Jung, H.S., Lim, D., Xu, Z., Kang, J.H., 2014. Quantitative compensation of grain-size effects in elemental concentration: a Korean coastal sediments case study. Estuar. Coast. Shelf Sci. 151, 69–77.

Kersten, M., Smedes, F., 2002. Normalization procedures for sediment contaminants in spatial and temporal trend monitoring. J. Environ. Monitor. 4, 109-115.

Kochhann, K.G.D., Holbourn, A., Kuhnt, W., Channell, J.E.T., Lyle, M., Shackford, J.K., Wilkens, R.H., Andersen, N., 2016. Eccentricity pacing of eastern equatorial Pacific carbonate dissolution cycles during the Miocene Climatic Optimum. Paleoceanograhy 31, 1176–1192.

Koller, M., Stahel, W.A., 2011. Sharpening Wald-type inference in robust regression for small samples. Computat. Stat. Data Anal. 55, 2504–2515.

Kvaček, Z., Teodoridis, V., 2007. Tertiary macrofloras of the Bohemian Massif: a review with correlations within Boreal and Central Europe. Bull. Geosci. 82, 383-408.

Laceby, J.P., Evrard, O., Smith, H.G., Blake, W.H., Olley, J.M., Minella, J.P.G., Owens, P.N., 2017. The challenges and opportunities of addressing particle size effects in sediment source fingerprinting: A review. Earth Sci. Rev. 169, 85-103.

Laskar, J., Robutel, P., Joutel, F., Gastineau, M., Correia, A.C.M., Levrard, B., 2004. A long-term numerical solution for the insolation quantities of the Earth. Astron. Astrophys. 428, 261–285.

Li, X.-J., Zan, J.-B., Yang, R.-S., Fang, X.N., Yang, S.-L., 2020. Grain-size-dependent geochemical characteristics of Middle and Upper Pleistocene loess sequences from the Junggar Basin: Implications for the provenance of Chinese eolian deposits. Palaeogeogr. Palaeoclimatol. Palaeoecol. 538, 109458. DOI: 10.1016/j.palaeo.2019.109458

Liebrand, D., Beddow, H.M., Lourens, L.J., Pälike, H., Raffi, I., Bohaty, S.M., Hilgen, F.J., Saes, M.J.M., Wilson, P.A., van Dijk, A.E., Hodell, D.A., Kroon, D., Huck, C.E., Batenburg, S.J., 2016. Cyclostratigraphy and eccentricity tuning of the early Oligocene through early Miocene (30.1-17.1 Ma): *Cibicides*

mundulus stable oxygen and carbon isotope records from Walvis Ridge Site 1264. Earth Planet. Sci. Lett. 450, 392–405.

Lojka, R., Drábková, J., Zajíc, J., Sýkorová, I., Franců, J., Bláhová, A., Grygar, T., 2009. Climate variability in the Stephanian B based on environmental record of the Mšec Lake deposits (Kladno-Rakovník Basin, Czech Republic). Palaeogeogr. Palaeoclimatol. Palaeoecol. 280, 78–93.

Lupker, M., France-Lanord, C., Lavé, J., Bouchez, J., Galy, V., Métivier, F., Gaillardet, J., Lartiges, B., Mugnier, J.-L., 2011. A Rouse-based method to integrate the chemical composition of river sediments: Application to the Ganga basin, J. Geophys. Res., 116, F04012. DOI: 10.1029/2010JF001947.

Lupker, M., France-Lanord, C., Galy, V., Lavé, J., Kudrass, H., 2013. Increasing chemical weathering in the Himalayan system since the Last Glacial Maximum. Earth Planet. Sci. Lett. 365, 243–252.

Mach, K., Teodoridis, V., Matys Grygar, T., Kvaček, Z., Suhr, P., Standke, G., 2014. An evaluation of paleogeography and paleoecology in the Most Basin (Czech Republic) and Saxony (Germany) from the late Oligocene to the early Miocene. N. Jahrbuch Geol. Paläontol. Abh. 272, 13–45.

Maechler, M., Rousseeuw, P., Croux, C., Todorov, V., Ruckstuhl, A., Salibian-Barreram, M., Verbeke, T., Koller, M., Conceicao, E.L.T., di Palma, M.A., 2019. Robustbase: Basic robust statistics R package version 0.93-5. URL http://CRAN.R-project.org/package=robustbase. Accessed 6 June, 2020.

Mann, M.E., Lees, J.M., 1996. Robust estimation of background noise and signal detection in climatic series. Clim. Change 33, 409–445.

Maronna, R.A., Martin, R.D., Yohai, V.J., 2006. Robust Statistics, Theory and Methods. Wiley, Chichester.

Marshall, N., Zeeden, C., Hilgen, F., Krijgsman, W., 2017. Milankovitch cycles in an equatorial delta from the Miocene of Borneo. Earth Planet. Sci. Lett. 472, 229–240.

Martinez, M., Deconinck, J.-F., Pellenard, P., Riquier, L., Company, M., Reboulet, S., Moiroud, M., 2015. Astrochronology of the Valanginian–Hauterivian stages (Early Cretaceous): Chronological

Journal Pre-proof

relationships between the Paraná–Etendeka large igneous province and the Weissert and the Faraoni events. Glob. Planet. Change 131, 158–173.

Matys Grygar, T., 2019. Comment on "Millennial-scale climate changes manifest Milankovitch combination tones and Hallstatt solar cycles in the Devonian greenhouse world". Geology 47, E487. DOI: 10.1130/G46452C.1.

Matys Grygar, T., Popelka, J., 2016. Revisiting geochemical methods of distinguishing natural concentrations and pollution by risk elements in fluvial sediments. J. Geochem. Explor. 170, 39–57.

Matys Grygar, T., Mach, K., Pruner, P., Schnabl, P., Laurin, J., Martinez, M., 2014. A lacustrine record of the early stage of the Miocene Climatic Optimum in Central Europe from the Most Basin, Ohře (Eger) Graben, Czech Republic. Geol. Mag. 151, 1013–1033.

Matys Grygar, T., Elznicová, J., Kiss, T., Smith, H.G., 2016. Using sedimentary archives to reconstruct pollution history and sediment provenance: The Ohře River, Czech Republic. Catena 144, 109–129.

Matys Grygar, T., Mach, K., Hošek, M., Schnabl, P., Martinez, M., Koubová, M., 2017a. Early stages of clastic deposition in the Most Basin (Ohře Rift, Czech Republic, Early Miocene): timing and possible controls. Bull. Geosci. 92, 337–355.

Matys Grygar, T., Hošek, M., Mach, K., Schnabl, P., Martinez, M., 2017b. Climatic instability before the Miocene Climatic Optimum reflected in a Central European lacustrine record from the Most Basin in the Czech Republic. Palaeogeogr. Palaeoclimatol. Palaeoecol. 485, 930–945.

Matys Grygar, T., Mach, K., Schnabl, P., Martinez, M., Zeeden, 2019a. Orbital forcing and abrupt events in a continental weathering proxy from central Europe (Most Basin, Czech Republic, 17.7–15.9 Ma) recorded beginning of the Miocene Climatic Optimum. Palaeogeogr. Palaeoclimatol. Palaeoecol. 514, 423–440.

Matys Grygar, T., Mach, K., Martinez, M., 2019b. Checklist for the use of potassium concentrations in siliciclastic sediments as paleoenvironmental archives. Sediment. Geol. 382, 75–84.

Meyers, S.R., 2014. Astrochron: An R Package for Astrochronology, https://cran.r-project.org/package=astrochron. Accessed 6 June, 2020.

Journal Pre-proof

Meyers, S.R., 2019. Cyclostratigraphy and the problem of astrochronologic testing. Earth Sci. Rev. 190, 190–223.

Miller, K.G., Baluyot, R., Wright, J.D., Kopp, R.E., Browning, J.V., 2017. Closing an early Miocene astronomical gap with Southern Ocean $\delta^{18}O$ and $\delta^{13}C$ records: Implications for sea level change. Paleoceanography 32, 600–621.

Nesbitt, H.W., Young, G.M., 1982. Early Proterozoic climates and plate motions inferred from major element chemistry of lutites. Nature 299, 715–717.

Ochoa, D., Sierro, F.J., Hilgen, F.J., Cortina, A., Lofi, J., Kouwenhoven, T., Flores, J.-A., 2018. Origin and implications of orbital-induced sedimentary cyclicity in Pliocene well-logs of the Western Mediterranean. Mar. Geol. 403, 150–164.

Pang, H.-L., Pan, B.-T., Garzanti, E., Gao, H.-S., Zhao, X., Chen, D.-B., 2018. Mineralogy and geochemistry of modern Yellow River sediments: Implications for weathering and provenance. Chem. Geol. 488, 76–86.

Pawlowsky-Glahn, V., Egozcue, J.J., Tolosana-Delgado, R., 2015. Modeling and Analysis of Compositional Data. Wiley, Chichester.

Profe, J., Zolitschka, B., Schirmer, W., Frechen, M., Ohlendorf, C., 2016. Geochemistry unravels MIS 3/2 paleoenvironmental dynamics at the loess–paleosol sequence Schwalbenberg II, Germany. Palaeogeogr. Palaeoclimatol. Palaeoecol. 459, 537–551.

Prokopenko, A.A., Hinnov, L.A., Williams, D.F., & Kuzmin, M.I., 2006. Orbital forcing of continental climate during the Pleistocene: a complete astronomically tuned climatic record from Lake Baikal, SE Siberia. Quat. Sci. Rev. 25, 3431-3457.

Rajchl, M., Uličný, D., Grygar, R., Mach, K., 2009. Evolution of basin architecture in an incipient continental rift: the Cenozoic Most Basin, Eger Graben (Central Europe). Basin Res. 21, 269–294.

R Core Team, 2019. R: A language and environment for statistical computing. R Foundation for Statistical Computing, Vienna, Austria. URL http://CRAN.R-project.org/package=robustbase. Accessed 6 June, 2020.

Journal Pre-proof

Reimann, C., Filzmoser, P., Fabian, K., Hron, K., Birke, M., Demetriades, A., Dinelli, E., Ladenberger, A., 2012. The concept of compositional data analysis in practice – Total major element concentrations in agricultural and grazing land soils in Europe. Sci. Tot. Environ. 426, 196–210.

Rousseeuw, P.J., van Driessen, K., 1999. A fast algorithm for minimum covariance determinant estimator. Technometrics 41, 212–223.

Schwarzacher, W., 2000. Repetitions and cycles in stratigraphy. Earth-Sci. Rev. 50, 51–75.

Sun, X., Fan, D., Liu, M., Tian, Y., Pang, Y., Liao, H., 2018a. Source identification, geochemical normalization and influence factors of heavy metals in Yangtze River Estuary sediment. Environ. Pollut. 241, 938–949.

Sun, W.-W., Zhang, E.-L., Liu, E.-F., Chang, J., Shen, J., 2018b. Linkage between Lake Xingkai sediment geochemistry and Asian summer monsoon since the last interglacial period. Palaeogeogr. Palaeoclimatol. Palaeoecol. 512, 71–79.

Tanaka, K., Watanabe, N., 2015. Size distribution of alkali elements in riverbed sediment and its relevance to fractionation of alkali elements during chemical weathering. Chem. Geol. 411, 12–18.

Thöle, H., Bornemann, A., Heimhofer, U., Luppold, F.W., Blumenberg, M., Dohrmann, R., Erbacher, J., 2019. Using high-resolution XRF analyses as sequence stratigraphic tool in a mudstone-dominated succession (Early Cretaceous, Lower Saxony Basin, Northern Germany). Deposit. Rec. 6, 236-258.

Thomson, D. J., 1982. Spectrum estimation and harmonic analysis. Proc. IEEE 70, 1055–1096.

Thomson, D. J., 1990. Quadratic-inverse spectrum estimates – applications to paleoclimatology. Philos. Trans. Royal Soc. London Ser. A–Math. Phys. Engin. Sci. 332, 539–597.

Tolosana-Delgado, R., von Eynatten, H., 2010. Simplifying compositional multiple regression: Application to grain size controls on sediment geochemistry. Comp. Geosci. 36, 577–589.

Tolosana-Delgado, R., McKinley, J., 2016. Exploring the joint compositional variability of major components and trace elements in the Tellus soil geochemistry survey (Northern Ireland). Appl. Geochem. 75, 263–276.

Journal Pre-proof

Uličný, D., Laurin, J., Čech, S., 2009. Controls on clastic sequence geometries in a shallow-marine, transtensional basin: The Bohemian Cretaceous Basin, Czech Republic. Sedimentology 56, 1077–1114.

van de Kamp, P.C., 2016. Potassium distribution and metasomatism in pelites and schists: how and when, relation to postdepositional events. J. Sediment. Res. 86, 683–711.

Vaughan, S., Bailey, R.J., Smith, D.G., 2011. Detecting cycles in stratigraphic data: Spectral analysis in the presence of red noise. Paleoceanography 26, PA4211. DOI: 10.1029/2011PA002195

von Eynatten, H., Tolosana-Delgado, R., Karius, V., Bachmann, K., Caracciolo, L., 2016. Sediment generation in humid Mediterranean setting: Grain-size and source-rock control on sediment geochemistry and mineralogy (Sila Massif, Calabria). Sediment. Geol. 336, 68–80.

Wampler, J.M., Krogstad, E.J., Elliott, W.C., Kahn, B., Kaplan, D.I., 2012. Long-term selective retention of natural Cs and Rb by highly weathered coastal plain soils. Environ. Sci. Technol. 46, 3837–3843.

Weedon G.P., 2003. Time Series Analysis and Cyclostratigraphy. Examining the Stratigraphic Records of Environmental Cycles. Cambridge University Press, Cambridge, UK.

Weedon, G.P., Page, K.N., Jenkyns, H.C., 2019. Cyclostratigraphy, stratigraphic gaps and the duration of the Hettangian Stage (Jurassic): insights from the Blue Lias Formation of southern Britain. Geol. Mag. 156, 1469-1509.

Yohai, V.J., 1987. High breakdown-point and high efficiency estimates for regression. Annals Stat. 15, 642–665.

Zeeden, C., Meyers, S. R., Lourens, L. J., Hilgen, F. J., 2015. Testing astronomically tuned age models, Paleoceanography 30, 369–383.

Journal Pre-proof

Table 1. Independent (explanatory) variables for LEFs of individual elements ratios in individual cores.

Table 2. Independent (explanatory) variables for RRes of individual element ratios in all three examined cores. Each variable is listed in the form of log-ratios without the respective normalising constants and with g(.) representing the geometrical mean. Regression coefficient is given for HK930.

Journal Pre-proof

Figure 1. The Most Basin and position of drill cores. Geological map was adopted from Andreani et al. (2014).

Figure 2. Examples of lithological corrections of K/Si ratio (panels A to C) and K/Rb (D to F) in HK930 sediments. K/Si (A), K/Si K/Si (B), and RRes (C) plot against Al/Si showing removal of grain size control. K/Rb plot against Fe concentration (D) and K/Rb LEF plot against Fe (E) and Al/Si (F).

Figure 3. Comparison of local enrichment factors (LEF) of all four tested element ratios in the HK930 drill core. Numbers 1 to 5 stand for prominent K minima used in local stratigraphy and depth-age models.

Figure 4. Raw and lithologically corrected K/Al (A) and K/Rb (B) ratios in HK930. Smoothing by 3 pt. median. Numbers 1 to 5 refer to local chemostratigraphy scheme for K# minima. K1 in K/Rb depth profiles seems split to separated minima. Not-numbered black rectangles highlight several other minima. Red arrow shows the beginning of the MCO according to Holbourn et al. (2015), Kochhann et al. (2016), and Matys Grygar et al. (2019a).

Figure 5. 2π-MTM spectral analyses of raw (A) and lithologically corrected (B and C) element ratios in HK930.

Figure 6. 2π-MTM spectral analyses of two explanatory variables used in LEF corrections.

Figure 7. Lateral correlation of K/Rb LEF in cores DU7, HK930, and DO656 (3pt. medians) compared with eccentricity and precession (Laskar et al., 2004). The eccentricity maxima used for matching corresponding K minima and constructing depth-age models are numbered 1 to 5. Vertical black lines

highlight some laterally correlated precession-controlled minima. The upper part of DO565 shows insufficient sampling density.

Figure 8. Lateral correlation of Mg/Al RRes in cores DU7, HK930, and DO656 (3pt. medians) compared with calculated obliquity (Laskar et al., 2004). The position of the K minima numbered 1 to 5 are shown. Vertical black rectangles are shown to highlight laterally correlated obliquity-controlled minima.

Journal Pre-proof

Table 1

Drill core	K/Al	K/Si	K/Rb	Mg/Al
HK930	Al/Si, $(Al/Si)^2$, Fe	Al/Si, $(Al/Si)^2$, Fe	Fe, Al/Si	Al/Si, Fe, Ca
DU7	Al/Si	Al/Si	Fe	Al/Si, Fe
DO565	Al/Si		Fe	Al/Si, Fe, Ca

Journal Pre-proof

Table 2

Response variable	Explanatory variables	R^2 in HK930
log(K/Al)	log(Zr/Rb), log(Si/g(Fe,Ca,Mg)), log(Fe/g(Ca,Mg)), log(Ca/Mg)	0.6093
log(K/Si)	log(Zr/Rb), log(Al/g(Fe,Ca,Mg)), log(Fe/g(Ca,Mg)), log(Ca/Mg)	0.7365
log(K/Rb)	log(Al/Si), log(Al/g(Fe,Ca,Mg)), log(Fe/g(Ca,Mg)), log(Ca/Mg)	0.6137
log(Mg/Al)	log(Zr/Rb), log(Si/g(Fe,Ca)), log(Fe/Ca)	0.6167

Journal Pre-proof

Conflict of interests

The authors declare no conflict of interests.

Journal Pre-proof

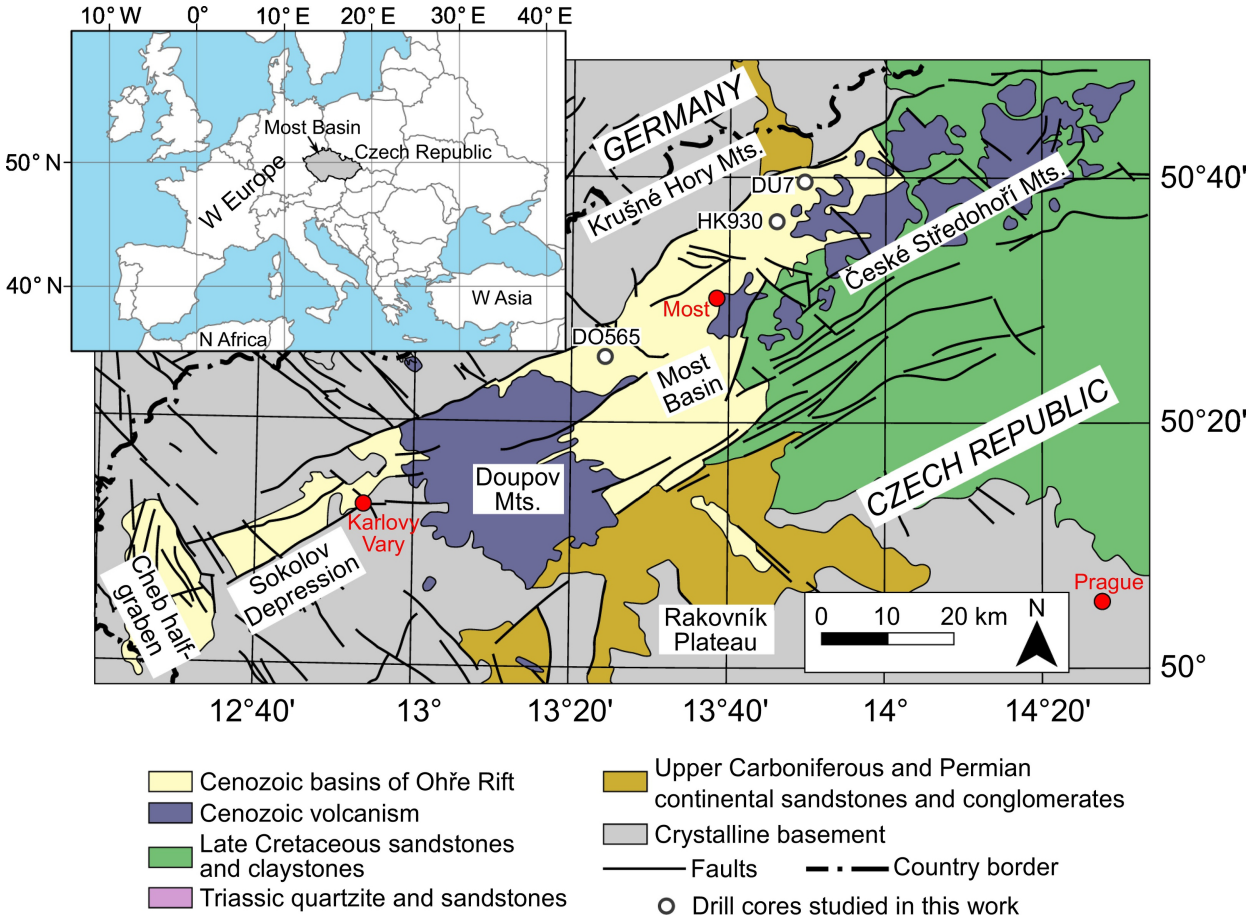
10° W
0°
10° E
20° E
30° E
40° E
50° N
40° N
Most Basin
Czech Republic
W Europe
W Asia
N Africa
GERMANY
Krušné Hory Mts.
DU7
HK930
České Středohoří Mts.
Most
DO565
Most Basin
CZECH REPUBLIC
Doupov Mts.
Karlovy Vary
Sokolov Depression
Cheb half-graben
Rakovník Plateau
Prague
0 10 20 km
N
50°40'
50°20'
50°
12°40'
13°
13°20'
13°40'
14°
14°20'
Cenozoic basins of Ohře Rift
Cenozoic volcanism
Late Cretaceous sandstones and claystones
Triassic quartzite and sandstones
Upper Carboniferous and Permian continental sandstones and conglomerates
Crystalline basement
Faults
Country border
Drill cores studied in this work

Figure 1

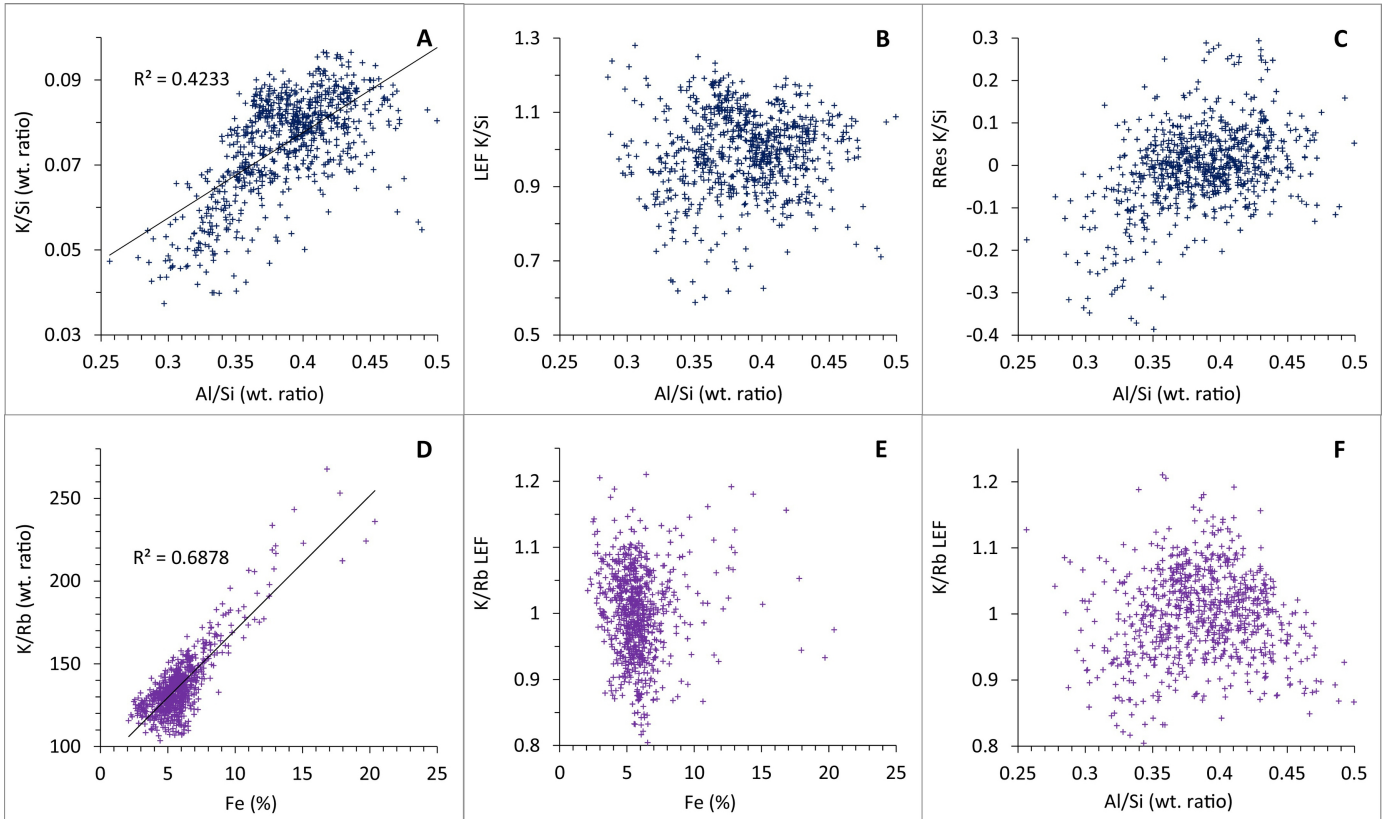
A
R² = 0.4233
K/Si (wt. ratio)
0.09
0.07
0.05
0.03
0.25
0.3
0.35
0.4
0.45
0.5
Al/Si (wt. ratio)
B
LEF K/Si
1.3
1.1
0.9
0.7
0.5
0.25
0.3
0.35
0.4
0.45
0.5
Al/Si (wt. ratio)
C
RRes K/Si
0.3
0.2
0.1
0
-0.1
-0.2
-0.3
-0.4
0.25
0.3
0.35
0.4
0.45
0.5
Al/Si (wt. ratio)
D
R² = 0.6878
K/Rb (wt. ratio)
250
200
150
100
0
5
10
15
20
25
Fe (%)
E
K/Rb LEF
1.2
1.1
1
0.9
0.8
0
5
10
15
20
25
Fe (%)
F
K/Rb LEF
1.2
1.1
1
0.9
0.8
0.25
0.3
0.35
0.4
0.45
0.5
Al/Si (wt. ratio)

Figure 2

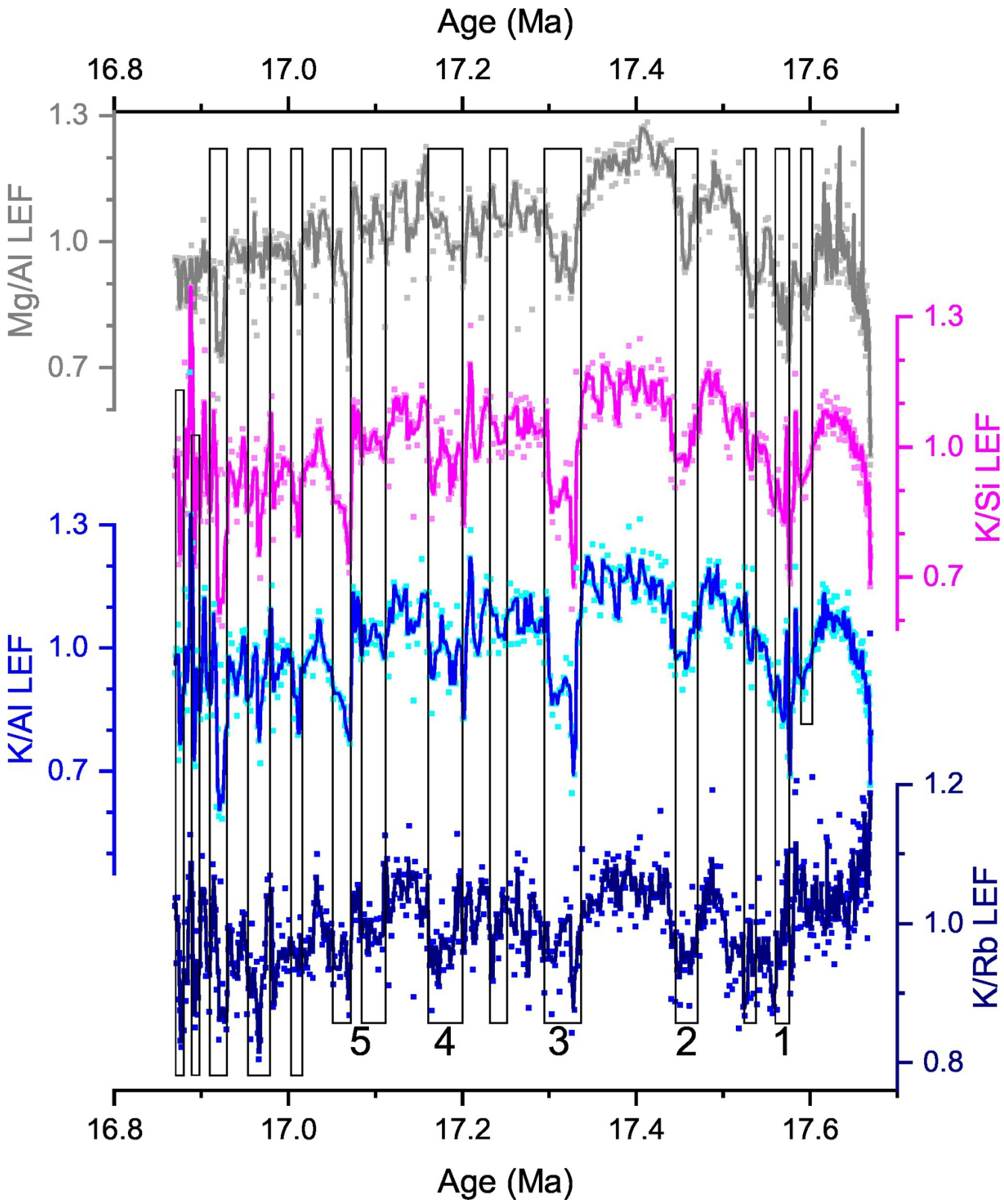
Age (Ma)
16.8
17.0
17.2
17.4
17.6
Mg/Al LEF
1.3
1.0
0.7
K/Si LEF
1.3
1.0
0.7
K/Al LEF
1.3
1.0
0.7
K/Rb LEF
1.2
1.0
0.8
5
4
3
2
1
16.8
17.0
17.2
17.4
17.6
Age (Ma)

Figure 3

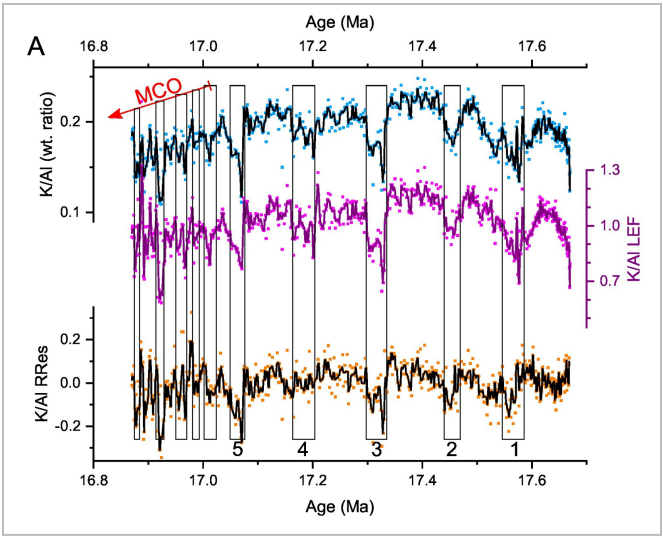
A
Age (Ma)
16.8
17.0
17.2
17.4
17.6
MCO
K/Al (wt. ratio)
0.2
0.1
1.3
1.0
0.7
K/Al LEF
K/Al RRes
0.2
0.0
-0.2
5
4
3
2
1

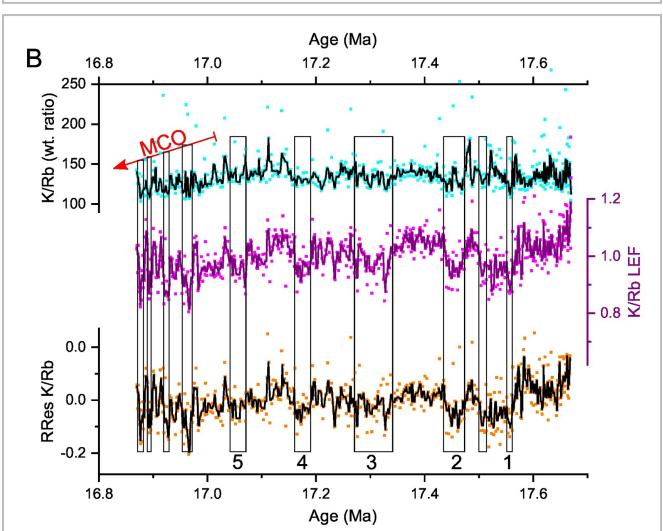
B
Age (Ma)
16.8
17.0
17.2
17.4
17.6
MCO
K/Rb (wt. ratio)
250
200
150
100
1.2
1.0
0.8
K/Rb LEF
RRes K/Rb
0.0
0.0
-0.2
5
4
3
2
1

Figure 4

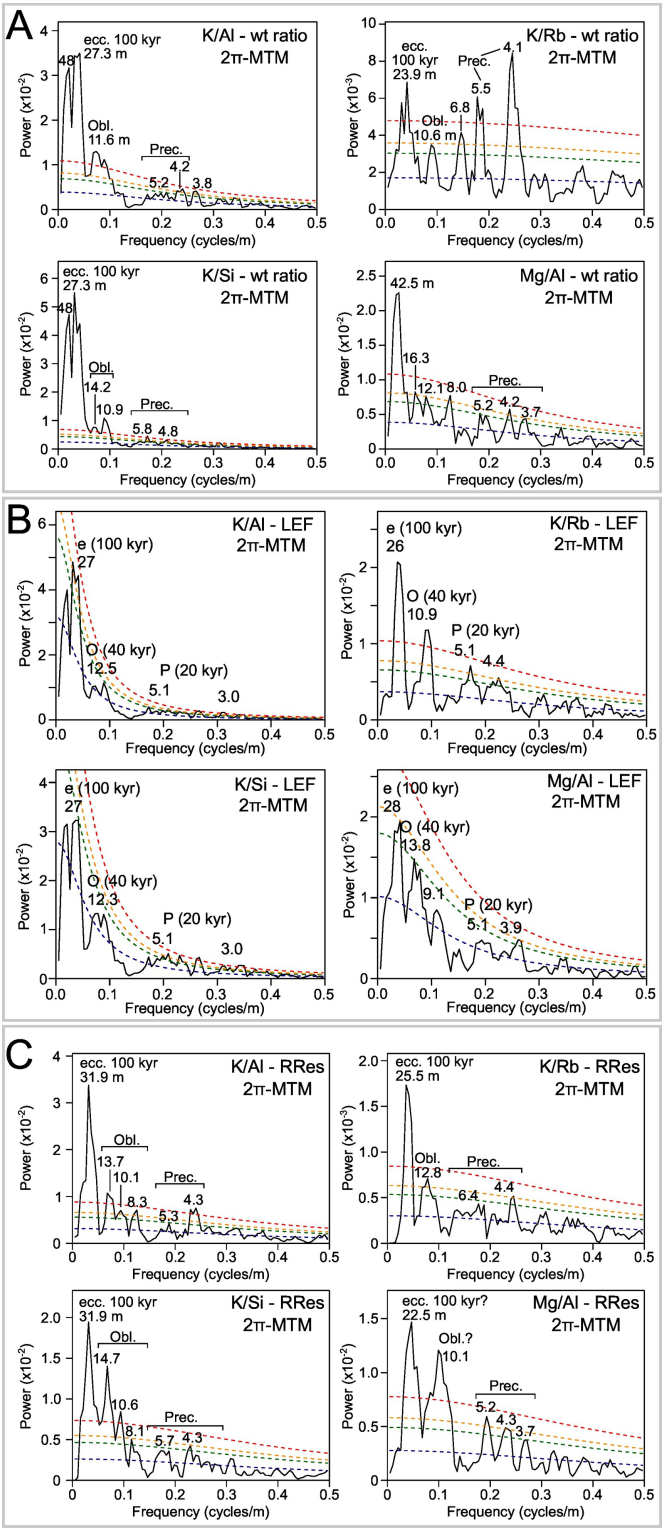
A
K/Al - wt ratio
2π-MTM
ecc. 100 kyr
27.3 m
48
Obl.
11.6 m
Prec.
4.2
5.2
3.8
K/Rb - wt ratio
2π-MTM
ecc.
100 kyr
23.9 m
Prec.
4.1
5.5
6.8
Obl.
10.6 m
K/Si - wt ratio
2π-MTM
ecc. 100 kyr
27.3 m
48
Obl.
14.2
10.9
Prec.
5.8
4.8
Mg/Al - wt ratio
2π-MTM
42.5 m
16.3
12.1
8.0
Prec.
5.2
4.2
3.7
Power (x10⁻²)
Power (x10⁻³)
Frequency (cycles/m)
B
K/Al - LEF
2π-MTM
e (100 kyr)
27
O (40 kyr)
12.5
P (20 kyr)
5.1
3.0
K/Rb - LEF
2π-MTM
e (100 kyr)
26
O (40 kyr)
10.9
P (20 kyr)
5.1
4.4
K/Si - LEF
2π-MTM
e (100 kyr)
27
O (40 kyr)
12.3
P (20 kyr)
5.1
3.0
Mg/Al - LEF
2π-MTM
e (100 kyr)
28
O (40 kyr)
13.8
9.1
P (20 kyr)
5.1
3.9
C
K/Al - RRes
2π-MTM
ecc. 100 kyr
31.9 m
Obl.
13.7
10.1
Prec.
8.3
5.3
4.3
K/Rb - RRes
2π-MTM
ecc. 100 kyr
25.5 m
Obl.
12.8
Prec.
6.4
4.4
K/Si - RRes
2π-MTM
ecc. 100 kyr
31.9 m
Obl.
14.7
10.6
Prec.
8.1
5.7
4.3
Mg/Al - RRes
2π-MTM
ecc. 100 kyr?
22.5 m
Obl.?
10.1
Prec.
5.2
4.3
3.7

Figure 5

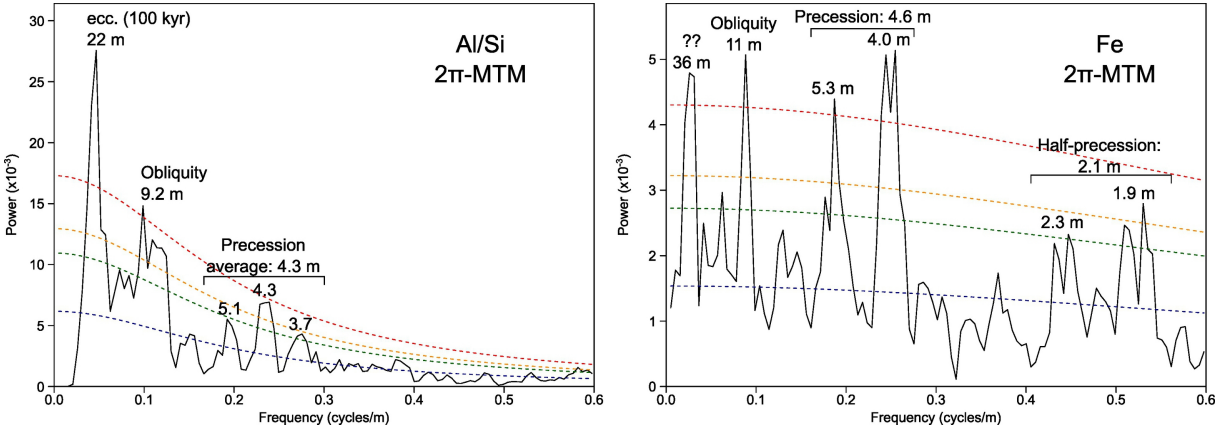
ecc. (100 kyr)
22 m
Al/Si
2π-MTM
Obliquity
9.2 m
Precession
average: 4.3 m
5.1
4.3
3.7
Power (x10⁻³)
Frequency (cycles/m)
??
36 m
Obliquity
11 m
Precession: 4.6 m
4.0 m
5.3 m
Fe
2π-MTM
Half-precession:
2.1 m
1.9 m
2.3 m
Power (x10⁻³)
Frequency (cycles/m)

Figure 6

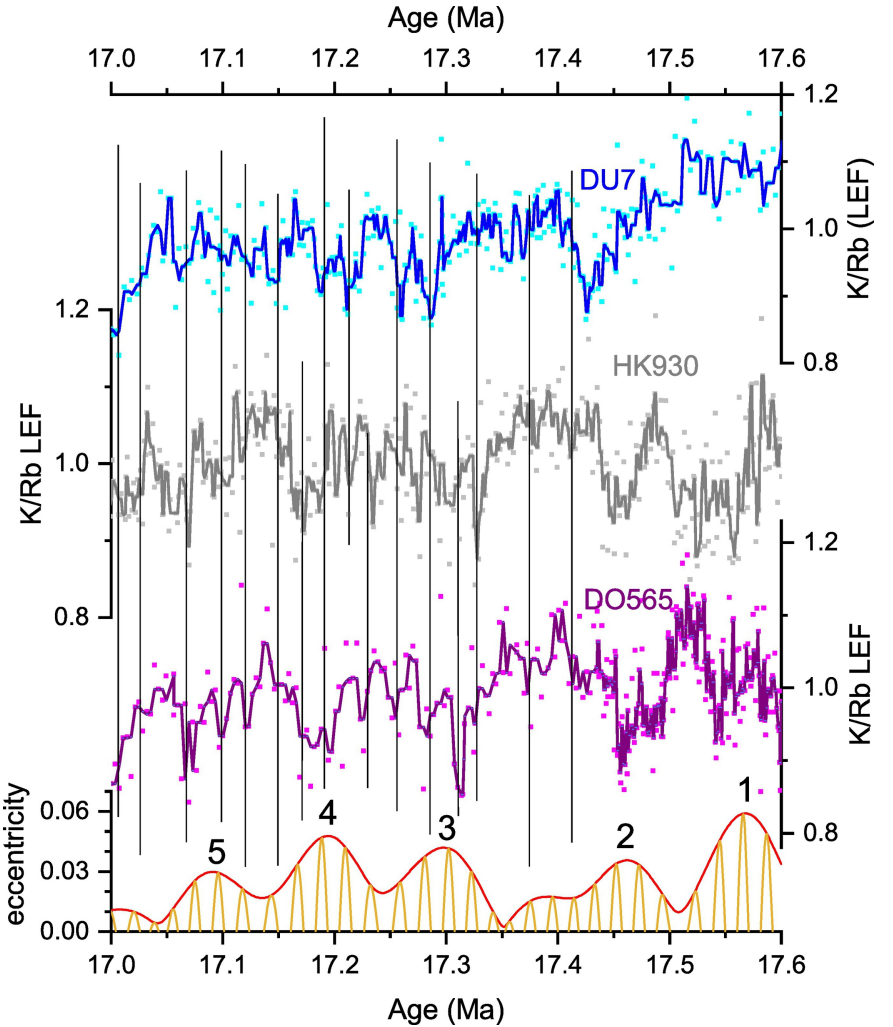
Age (Ma)
17.0
17.1
17.2
17.3
17.4
17.5
17.6
DU7
HK930
DO565
K/Rb (LEF)
K/Rb LEF
1.2
1.0
0.8
eccentricity
0.06
0.03
0.00
1
2
3
4
5

Figure 7

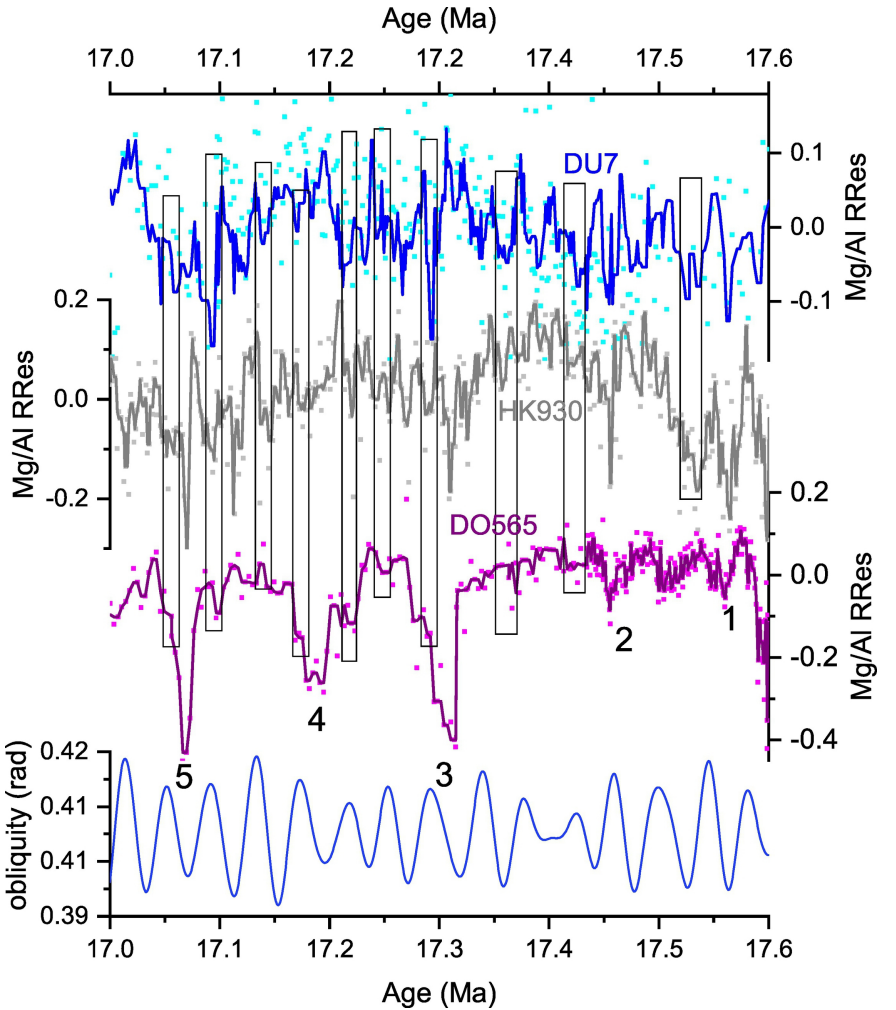
Age (Ma)
17.0
17.1
17.2
17.2
17.4
17.5
17.6
DU7
HK930
DO565
Mg/Al RRes
0.1
0.0
-0.1
0.2
0.0
-0.2
0.2
0.0
-0.2
-0.4
1
2
3
4
5
obliquity (rad)
0.42
0.41
0.41
0.39
17.0
17.1
17.2
17.3
17.4
17.5
17.6
Age (Ma)

Figure 8